Behaviour of fission products in UO_2
Experimental characterization of the Cs-I-UO_2 model system at high temperature

Rochedy, M.; Klosek, V.; Riglet-Martial, C.; Onofri-Marroncle, C.; Drouan, D.; Reyes, D.; Bienvenu, P.; Roure, I.; Cabié, M.; More Authors

DOI
10.1016/j.jnucmat.2023.154450

Publication date
2023

Document Version
Final published version

Published in
Journal of Nuclear Materials

Journal of Nuclear Materials 581 (2023) 154450

Contents lists available at ScienceDirect

Journal of Nuclear Materials

journal homepage: www.elsevier.com/locate/jnucmat

Behaviour of fission products in UO_2: Experimental characterization of the Cs-I-UO_2 model system at high temperature

M. Rochedy [a,b], V. Klosek [a,*], C. Riglet-Martial [a], C. Onofri-Marroncle [a], D. Drouan [a], D. Reyes [a], P. Bienvenu [a], I. Roure [a], M. Cabié [c], L. Amidani [d], J. Léchelle [a], M-A. Pinault-Thaury [e]

[a] CEA, DES, IRESNE, DEC, Cadarache, Saint-Paul-Lez-Durance F-13108, France
[b] Radiation Science & Technology Department, Faculty of Applied Sciences, Delft University of Technology, Mekelweg 15, Delft 2629 JB, the Netherlands
[c] CP2M, Université Aix-Marseille, Marseille 13013, France
[d] ESRF, The European Synchrotron, CS40220, Grenoble 38043 CEDEX 9, France
[e] UVSQ, CNRS, GEMaC, Université Paris-Saclay, Versailles 78000, France

ARTICLE INFO

Keywords:
Nuclear fuel
Iodine induced stress corrosion cracking (I-SCC)
Iodine
Caesium
Thermodynamics
Microstructure
Speciation

ABSTRACT

The interactions of iodine and caesium in UO_2 have been investigated. For this purpose, implanted UO_2 samples were thermally treated (4h at 900°C or 1h at 1200°C) under controlled atmosphere (0.03% H_2O/H_2) and then characterized by several experimental techniques for their structural and chemical studies. Thermodynamic calculations were also performed in order to optimize heat treatment conditions before performing tests, and to help in the interpretation of results afterwards. The sample characterizations after thermal treatments reveal the presence of bubbles and precipitates (mean diameter around 10 - 20 nm) and have allowed to clearly identify the presence of CsI in these bubbles which is in agreement with the calculations. The chemical form of the observed precipitates is not well defined yet, due to the lack of experimental reference spectra, but they consist very likely of caesium uranates, as predicted by the thermodynamic calculations.

1. Introduction

A major phenomenon to be considered during the transient operation of a Pressurized Water Reactor (PWR) is Iodine induced Stress Corrosion Cracking (I-SCC) [1]. Indeed, when a significant increase in power occurs, the temperature in the center of the pellet rises up. This increase of temperature favours the release of some Fission Products (FPs), including iodine, which migrate through fuel cracks toward the cladding. At the same time, the stress level in the cladding also increases. The combination of these three phenomena can lead to I-SCC and may cause cladding failure. Thus, integrity of the first containment barrier can be questioned. Research and development programs are devoted to I-SCC in order to improve the understanding of the mechanisms leading to cladding failures and to help optimize plant operational procedures and fuel management schemes.

One of the key parameters of the I-SCC is iodine speciation. The chemical form of iodine affects its corrosiveness with respect to the material of the cladding (Zircaloy). Various parameters may affect iodine speciation, such as temperature (T), oxygen partial pressure (pO_2) and the presence of other chemical elements. Previous thermodynamical studies have determined that the chemical model system to take into account is I-Cs-Te-Mo in UO_2 [2]. Iodine can interact with both Cs, to form CsI, and Te to form compounds such as TeI_x (x = 2 or 4) which are highly corrosive for Zr, unlike CsI. Moreover, Cs, Te and I were detected simultaneously at a fuel pellet periphery, in the vicinity of the cladding, of a power-ramped UO_2 irradiated fuel [3]. In turn, Mo is an abundant FP likely to interact with Cs to form very stable compounds and consequently affects the chemical equilibria involving I. Some

Abbreviations: dpa, displacement per atom; EDX, energy dispersive X-Ray analysis; EELS, electron energy loss spectroscopy; FP, fission product; HAADF, high angle annular dark field; HC, high concentration; IC, intermediate concentration; I-SCC, iodine induced stress corrosion cracking; LC, low concentration; pO_2, oxygen partial pressure; PWR, pressurized water reactor; SEM, scanning electron microscopy; SIMS, secondary ion mass spectrometry; STEM, scanning transmission electron microscopy; T, temperature; TEM, transmission electron microscopy; v, version; XANES, X-ray absorption near edge spectroscopy; XAS, X-ray absorption spectroscopy.

* Corresponding author.
E-mail address: vincent.klosek@cea.fr (V. Klosek).

https://doi.org/10.1016/j.jnucmat.2023.154450
Received 20 January 2023; Received in revised form 21 March 2023; Accepted 12 April 2023
Available online 13 April 2023

previous studies have investigated the diffusion mechanisms of these elements in UO_2, as well as some microstructural evolutions, as a function of temperature and controlled atmosphere [4–9]. However, few experimental data are available as to the chemical form of these FPs in UO_2 and as a function of temperature and pO_2.

As stated before, Cs and I can form CsI which is a stable compound. This compound was observed on the inner surface of the cladding of a fuel that had undergone a power ramp [10]. However, Shann and Olander [11] showed by means of mechanical tests that CsI cannot cause cracks by I-SCC. Indeed, the reaction of CsI with zirconium is not favourable from a thermodynamic point of view. Different mechanisms have been suggested to explain the corrosive environment caused by iodine. It was mentioned that iodine could be transported toward the gap or to the pellet - cladding interface under the stable form CsI, and then the latter could be decomposed by radiolysis, releasing aggressive iodine that could react with Zr [12]. Wood [13] proposed a mechanism of iodine adsorption on the cladding surface causing a decrease in the surface energy and an embrittlement of Zr-Zr bonds. Cox and Haddad [14] suggested that the adsorbed species is a zirconium iodide, $ZrI_{4(g)}$, which is formed before adsorbing on the surface of Zircaloy. Another proposed mechanism involves the decomposition of CsI and the formation of caesium oxides or other more complex compounds at higher oxygen partial pressure [15]. For example, one of the reactions proposed to generate iodine with CsI is the following [16]:

$$CsI_{(s)} + \frac{1}{2}O_{2(g)} + \frac{1}{2}UO_{2(s)} = \frac{1}{2}Cs_2UO_{4(s)} + I_{(g)}$$

This mechanism suggests that CsI could dissociate under specific conditions of temperature (T) and oxygen partial pressure (pO_2).

This paper presents a separate-effects approach whose objective is to study the chemical interaction between I and Cs in UO_2 under controlled T and pO_2 conditions. For that purpose, I and Cs were ion-implanted into UO_2 samples. The implanted samples were subsequently annealed. The heat treatment conditions were chosen to be representative of the temperature at the center of a pellet during irradiation under normal PWR conditions (between 900 and 1200°C), and the pO_2 was fixed in order to be representative of stoichiometric UO_2. The originality of this work relies on its methodology coupling an experimental approach with thermodynamic modelling. Thermodynamic calculations aim at both dimensioning the heat treatment conditions before the experiment, and helping in the interpretation of the characterization results afterwards. The experimental work is based on a cross-analysis of information acquired by several complementary experimental characterization techniques: Scanning Electron Microscopy (SEM), Transmission Electron Microscopy (TEM) in conventional or scanning mode coupled with Energy Dispersive X-ray (EDX) and Electron Energy Loss Spectroscopy (EELS), Secondary Ion Mass Spectrometry (SIMS) and X-ray Absorption Spectroscopy (XAS). These techniques allowed determining as precisely as possible the microstructural evolution as well as the chemical forms of caesium and iodine.

2. Material and methods

2.1. Sample preparation

2.1.1. UO_2 samples

A 16 mm thick and 8 mm diameter depleted UO_2 pellet (0.3 at.% of ^{235}U) was prepared in the UO_2 Laboratory (CEA Cadarache, France) using a UO_2 powder metallurgy process. The powder was uniaxally cold pressed under 400 MPa and then sintered at 1950 K for 4 h under Ar + 5% H_2 atmosphere leading to a stoichiometric material. Then, discs with a thickness around 1 mm were cut from the central part of the pellet and underwent a mechanical polishing with a final step performed with a 0.02 µm colloidal silica suspension in order to minimize the polishing superficial impact. The polished specimens were finally annealed at 1400°C during 4 h under Ar + 5 % H_2, this latter thermal treatment aiming at removing the stress and defects induced by the polishing step.

2.1.2. Cs and I implantations

The samples were implanted at room temperature with 800 keV ^{133}Cs ions and 800 keV ^{127}I ions at IP2I (Institut de Physique des 2 Infinis in Lyon, France) using the IMIO400 accelerator facility. Preliminary simulations of Cs and I implantation profiles were performed using the mode "Full Damage Cascades" of SRIM 2013 software [17]. A density of 10.7 g/cm^3 was considered for UO_2 and displacement energies were set to 40 eV for uranium atoms and 20 eV for oxygen atoms [18]. The calculated depth profiles of Cs and I are similar. They show Gaussian concentration distributions with a maximum at a projected range (Rp) of 140 nm and with a maximum implantation depth around 300 - 350 nm (Fig. 1). Table 1 summarizes the different fluences used in this study and the atomic concentrations, determined from SRIM calculations. Different fluences were adjusted to reach different concentration orders: (i) high fluences corresponding to two ([Cs], [I]) couples (HC: High Concentrations and IC: Intermediate Concentrations), in order to ensure the feasibility of the analyses; (ii) low fluences corresponding to one ([Cs], [I]) couple (LC: Low Concentrations), to be more representative of FP concentrations in a spent fuel at a burnup close to 7 at.%. The corresponding concentrations of I and Cs for LC were estimated using the following empirical formula from [2], giving the typical composition of an irradiated UO_2 fuel:

- [I] (mol/mol UO_2) = $1.31 \cdot 10^{-4} \cdot \tau_c$;
- [Cs] (mol/mol UO_2) = $1.7 \cdot 10^{-3} \cdot \tau_c$ where τ_c is the burnup in at.%.

2.1.3. Thermal treatment

Thermal treatments were performed in a sintering furnace (internal structure made of tungsten, maximal temperature of 1700°C). Oxygen partial pressure (pO_2) was adjusted by using a (H_2O, H_2) mixture with a H_2O/H_2 molar ratio of 0.03%. This gas composition has been chosen to ensure a UO_2 stoichiometry close to 2.000. Two thermal treatment conditions were studied: 4 h at 900°C with $pO_2 = 7 \cdot 10^{-24}$ atm and 1h at 1200°C with $pO_2 = 2 \cdot 10^{-19}$ atm.

This furnace allows to quickly set up the heat treatments, however the cooling rate cannot be controlled and is quite slow (approx. -6°C/min), which may lead to phase transformations during the return to ambient temperature if some species still have sufficient mobility.

2.2. Computational methods

Thermodynamic calculations aim both at dimensioning and optimizing the thermal treatment conditions before the experiment, and at

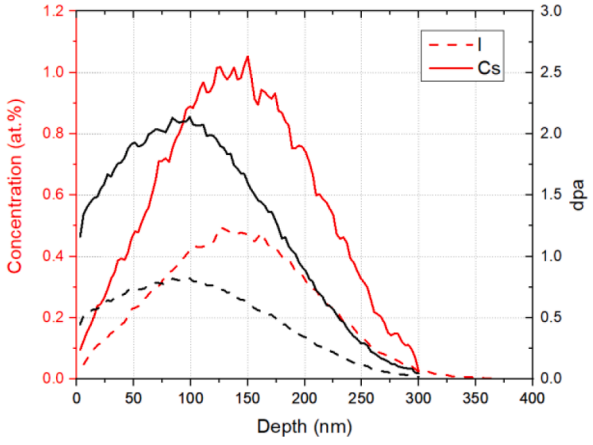

Fig. 1. Concentration depth profiles (in red) and displacements per atom (dpa) as a function of the implantation depth (in black), as calculated by SRIM for sample IC.

Table 1
Fluences of caesium and iodine implanted in UO_2 samples and corresponding calculated concentration at Rp – HC, IC and LC refer to high, intermediate and low concentration.

	Cs fluence (at/cm^2)	[Cs] at Rp (at. %)	I fluence (at/cm^2)	[I] at Rp (at. %)
HC	$2.5 \cdot 10^{16}$	2	$1.3 \cdot 10^{16}$	1
IC	$1.3 \cdot 10^{16}$	1	$6.0 \cdot 10^{15}$	0.5
LC	$5.0 \cdot 10^{15}$	0.4	$2.5 \cdot 10^{14}$	0.02

helping the interpretation of the characterization results.

Two databases were used for thermodynamic calculations: TAF-ID version 11 and SGPS version 13.1. The TAF-ID database [19] developed by the Nuclear Energy Agency (NEA) of the Organisation for Economic Co-operation and Development (OECD) is the result of an international collaboration, and is currently the most comprehensive database on fuel thermochemistry. It can be used with Thermo-Calc software. Calculations with FactSage were carried out with one of its associated databases, the pure substances database (SGPS) maintained by the Scientific Group Thermodata Europe (SGTE) [20]. These two databases were used to keep a critical eye on the calculation results. Indeed, we noted discrepancies between these two databases: on the one hand, compounds of potential interest for our study were sometimes missing, as the development of these databases is still in progress, and on the other hand, these databases sometimes refer to different sources from literature, with slightly different expressions of thermodynamic functions.

For all the calculations, only T and pO_2 were varied. The total gas pressure was taken equal to 1 bar and the concentrations of the elements (for this study: Cs and I) corresponded to the implanted concentrations at Rp (Table 1).

2.3. Characterizations

Table 2 summarizes the various characterizations performed on the resulting samples, according to their Cs and I concentrations.

2.3.1. Scanning Electron Microscopy (SEM)

Observations and analyses were performed using a SEM FEG (Field Emission Gun) of type Nova Nanosem 450. They were carried out with a working distance between 4.7 mm and 5.1 mm, an acceleration voltage of 15 kV and using the CBS (Circular Back Scattering) detector: secondary and backscattered electrons were detected simultaneously.

In addition to studying the implanted surface, cross sections (normal to the implanted surface) of selected samples were made to study the microstructure evolution as a function of depth. These cross-sections were prepared by first cutting the samples perpendicularly to their implanted surfaces. Each part was then glued along the implanted faces to a non-implanted UO_2 sample. Next, the resulting samples were embedded into resin. The whole system was finally polished and then observed by SEM.

2.3.2. Transmission Electron Microscopy (TEM)

Lamellae of implanted samples were prepared by means of a Focused Ion Beam (FIB). These preparations were done by using a dual-beam FIB Helios 600 NanoLab device at the Centre Pluridisciplinaire de Microscopies et Microanalyses (CP2M in Marseille, France). In order to obtain lamellae that can be analyzed by TEM, several steps were necessary. A layer of Pt was first deposited on the area of interest on the sample surface in order to protect the implanted area during FIB operations. Two trenches were then dug with a Ga^+ ion beam, on each side of the lamella. Then the lamella was cut off and removed from the sample, and finally thinned and cleaned with the Ga^+ ion beam using decreasing currents and energies. The thickness of each lamella was determined using Energy filtered transmission electron microscopy (EFTEM) maps, resulting in an average of 50 nm in the observation area.

Table 2
Summary of the characterizations performed on each type of Cs and I concentration – HC, IC and LC refer to high, intermediate and low concentration.

	Characterizations
HC	XAS, SEM, TEM
IC	SIMS
LC	XAS, SEM

The observations and analyses of the obtained lamellae were performed in the LECA STAR facility (CEA Cadarache, France) on a FEI TALOS FEG TEM in conventional and in STEM (Scanning Transmission Electron Microscopy) modes. HAADF (High Angle Annular Dark Field) detector was also used. Additional EDX and EELS analyses have been carried out in order to get information on the speciation of the chemical elements. The data processing for EDX and for EELS was performed with the Velox software (Thermo Fisher Scientific) and the GMS software (Gatan), respectively.

TEM images provide information on objects (bubbles, cavities, precipitates…) which are present in the implanted part of the lamella. The cavities and bubbles in conventional TEM mode are revealed by changing the focus conditions of the objective lens: they appear as white spots in underfocused conditions and as black spots in overfocused conditions. It should be noticed that the bubbles or cavities are not perceptible in the focusing condition [21]. The precipitates were highlighted by diffraction contrast. Unlike bubbles, precipitates are visible in focus and sometimes, depending on the diffraction conditions, Moiré fringes can be observed.

FIB preparation leads to the formation of additional sub-nanometric vacancy type objects and small dislocation loops (around 2 nm in diameter). The vacancy type objects are present in our samples at about 10^{24} m^{-3} and measure about 0.4 nm in diameter. For nanometric or sub-nanometric objects (such as those induced by the FIB), the measured size strongly depends on the level of defocusing applied, which in turn is linked to the observation conditions (electron source, magnification...) [22–24]. For all samples, object sizes were measured for focusing conditions of ±200 - 300 nm.

2.3.3. Secondary Ion Mass Spectrometry (SIMS)

The SIMS analysis were performed with dynamic magnetic sector SIMS, on a shielded IMS6f-CAMECA instrument at LECA STAR facility, in order to measure the depth profiles of Cs and I in as-implanted and annealed samples. In routine analysis, the raster size was 120×120 μm^2 for Cs and 150×150 μm^2 for I and the analyzed zone was restricted to a diameter of 60 μm in order to avoid crater sidewall effects. The depth of the resulting SIMS crater, P_{crater}, was measured by a confocal chromatic type profilometer, MICROMESURE 2 from STIL.

The analysis chamber was kept under high vacuum (~10^{-8} mbar). As the SIMS technique is mostly used to detect impurities, measurements were performed with parameters allowing high sensitivities. Namely, low mass resolution (LMR) settings were used together with Cs^+/M^- and O_2^+/M^+ configurations: positive primary ions with Cs^+ or O_2^+ source and detection of negative or positive secondary ions, respectively. Therefore, the measurements were carried out in two stages: negatively charged ions, $^{127}I^-$ for iodine and $^{16}O_2^-$ for the matrix reference, were collected by sputtering with Cs^+ ions, $^{133}Cs^+$ for caesium and $^{238}U^{16}O_2^+$ for the matrix reference, were collected by sputtering O_2^+ ions. The impact energy of the Cs^+ and O_2^+ primary ions was of 15 keV and 10 keV, respectively. Secondary ions were detected in the positive/negative mode by biasing the sample to -5 kV for the measurement of negative secondary ions and +5 kV for the measurement of positive secondary ions. By using a primary intensity of 30 and 40 nA for Cs^+ and O_2^+ primary beam, sputtering rates of around 0.8 nm/s and 0.3 nm/s in UO_2 matrix were obtained, respectively. For each sample and element of

interest (iodine and caesium), two replicate analyses were performed with these optimized experimental conditions. Error on depth measurements can be estimated to ± 20 nm, and the relative error on concentrations to 25%.

The chronograms of each element of interest, X (iodine and caesium in our case), were registered in intensity (count per second) over time. To convert them into depth profiles (element concentration over depth), the time was firstly converted into depth by applying the factor P_{crater}/t_{total}, where t_{total} is the total acquisition time. Then, we used the RSF method (Relative Sensitivity Factors) to convert intensities into concentrations as described hereafter. The RSF of the element of interest, X, is deriveded from the analysis of the as-implanted samples with a known implantation dose φ of X thanks to Eq. (1) [25]:

$$RSF(X) = \frac{\varphi \times \overline{I_{mat}} \times n_c}{[\sum I_X - (I_b \times n_c)]P_{crater}} \left(at/cm^3\right) \quad (1)$$

With

φ : implantation fluence of X (ions/cm^2);
$\overline{I_{mat}}$: average signal value of the matrix element (^{16}O or $^{238}U^{16}O$ in our case);
I_X : signal value of the element of interest, X ($^{127}I^-$ or $^{133}Cs^+$ in our case);
I_b : background intensity (estimated using the last analysis points);
n_c : number of cycles;
P_{crater} : depth of the SIMS crater (cm).

From our work, the RSF values of iodine and caesium in UO_2 are (2.1 ± 0.4) x 10^{22} and (9.1 ± 2.3) x 10^{22} at/cm^3, respectively. The intensity signal of the element of interest, X, was converted into concentration thanks to the RSF value and the normalized intensity of the element of interest with Eq. (2):

$$[X] = \frac{I_{norm}(X) \times RSF(X)}{x \times N_A \times \frac{\rho}{M}} \ (at.\%) \quad (2)$$

with

$I_{norm}(X)$: normalized intensity of the element of interest X (= I_X/I_{mat});
x : number of atoms per formula unit (= 3 for UO_2);
N_A : Avogadro number = 6.02×10^{23} /mol;
ρ : density of UO_2 = 10.7 g/cm^3;
M : molar mass of UO_2 = 270.03 g/mol.

2.3.4. XANES spectroscopy

XANES experiments were performed at room temperature on the ID26 beamline at ESRF (Grenoble, France) at the L_3 edges of Cs (E_0=5012 eV) and I (E_0=4556 eV) on the HC samples. Measurements were carried out on half disks confined in Kapton. HERFD-XANES spectra were collected using five Si (311) bent crystals (bending radius of 1000 mm) mounted on the emission spectrometer available on ID26 beamline. This method provides highly accurate XANES data on these very diluted elements within a highly absorbing UO_2 matrix and minimizes the influence of other absorption cross sections in the considered energy ranges (mainly U M edges). The emission spectrometer was tuned to the $L_{\alpha1}$ emission line of iodine (3942 eV) or caesium (4290 eV). Spectra were recorded in a continuous quick scan mode of both monochromator and undulator gap over the request energy ranges. A helium bag was inserted between the sample, the crystals and the detector to avoid beam absorption by air.

The caesium iodine, CsI, was also measured as a reference compound. Since no pure Cs_2UO_4 reference sample was available for measurements, a Cs L_3 reference spectrum for Cs_2UO_4 was simulated from its reported crystal data [26] using the FDMNES code [27], applying the finite difference method to solve the Schrödinger equation in the local density approximation, and considering spin-orbit coupling.

Athena software [28] was used to normalize the XANES spectra.

3. Results

3.1. Thermodynamic calculations

Fig. 2 shows the predominance diagrams calculated with FactSage and the SGPS v13.1 database (a) and with Thermo-Calc and TAF-ID v11 database (b). The calculations were performed for the HC concentrations of elements (Table 1). No significant difference could be deduced between the predominance diagrams obtained for LC samples and those obtained for HC, as long as temperatures lower than 1200°C were considered. The red dotted line represents the pO_2 evolution with T of the gas mixture H_2 + 300 vol ppm H_2O and the red spots correspond to the experimental thermal treatment conditions.

According to these calculations, caesium uranate, Cs_2UO_x (with x=4 from SGPS database and x=3.5 from TAF-ID database), and CsI should form during a heat treatment at 900°C. At this temperature, CsI would be either under liquid form in equilibrium with its gaseous form or under its gaseous form only depending on total pressure and composition in the bubbles. In fact, as any liquid-gas equilibrium, increase in local total pressure and/or increase in iodine content in a bubble stabilizes the liquid phase whereas decrease in local total pressure and /or decrease in iodine content in the bubbles stabilizes the gas phase. The calculations predict the formation of a gas phase mainly composed of Cs, Cs_2 and CsI during a heat treatment at 1200°C. Therefore, if a sufficiently fast cooling down to room temperature can be carried out so that the system does not have enough time to evolve during cooling, we expect to observe Cs_2UO_x and CsI after the thermal treatment at 900°C, and CsI and condensed (metallic) Cs after the treatment at 1200°C.

3.2. Evolution of UO_2 microstructure with I and Cs implantation

3.2.1. SEM observations

Fig. 3 shows the surface of HC samples before (b) and after thermal treatments (900°C (c) and 1200°C (d)). After implantation (Fig. 3 (b)), the surface exhibits hollowed grain boundaries and many micron-sized pores (which appear as large black dots on Fig. 3 (a)–(d)). These observations are similar to that on the surface of a pristine (non-implanted) UO_2 reference sample (Fig. 3 (a)). Therefore, no evolution of the microstructure due to the implantation process can be observed at this scale. After thermal treatments, little black dots appear at the surface, inside grains (Fig. 3 (b) and (c)), which are identified as open bubbles (white arrows). Their presence seems to indicate a significant gas release during the thermal treatments. It should be noticed that such open bubbles are also observed for the heat treated LC samples, but with a lower density.

Cross-section of samples annealed at 1200°C were prepared for the two types of concentration. Only the image of the HC sample is shown here (Fig. 3 (e)). It shows the presence of many other bubbles (diameter: 30 – 100 nm) located down to 250 nm beneath the surface.

3.2.2. TEM characterization

Following these observations, TEM analyses were performed in order to study the microstructural features at a finer scale and the bubbles shown previously. Figs. 4–6 present bright field images obtained on the as-implanted HC sample, after an annealing at 900°C and after an annealing at 1200°C respectively.

As-implanted sample.

The as-implanted sample shows a defect-rich zone (mainly dislocation loops up to a size of 10 nm in diameter) between 250 and 400 nm in depth (Fig. 4). The FIB preparation induced also many small dislocation loops (density equal to (5.3 ± 0.8)·10^{22} m^{-3} with a diffraction vector along the <111> direction and an average diameter of 1.8 nm; data obtained in a fresh sample), but no dislocation line or loop larger than 5 nm. The defects observed in this sample are therefore mainly due to the implantation process of iodine and caesium ions in UO_2. Sub-nanometric vacancy type objects (density: (1.8±0.3)·10^{24} m^{-3}, average diameter:

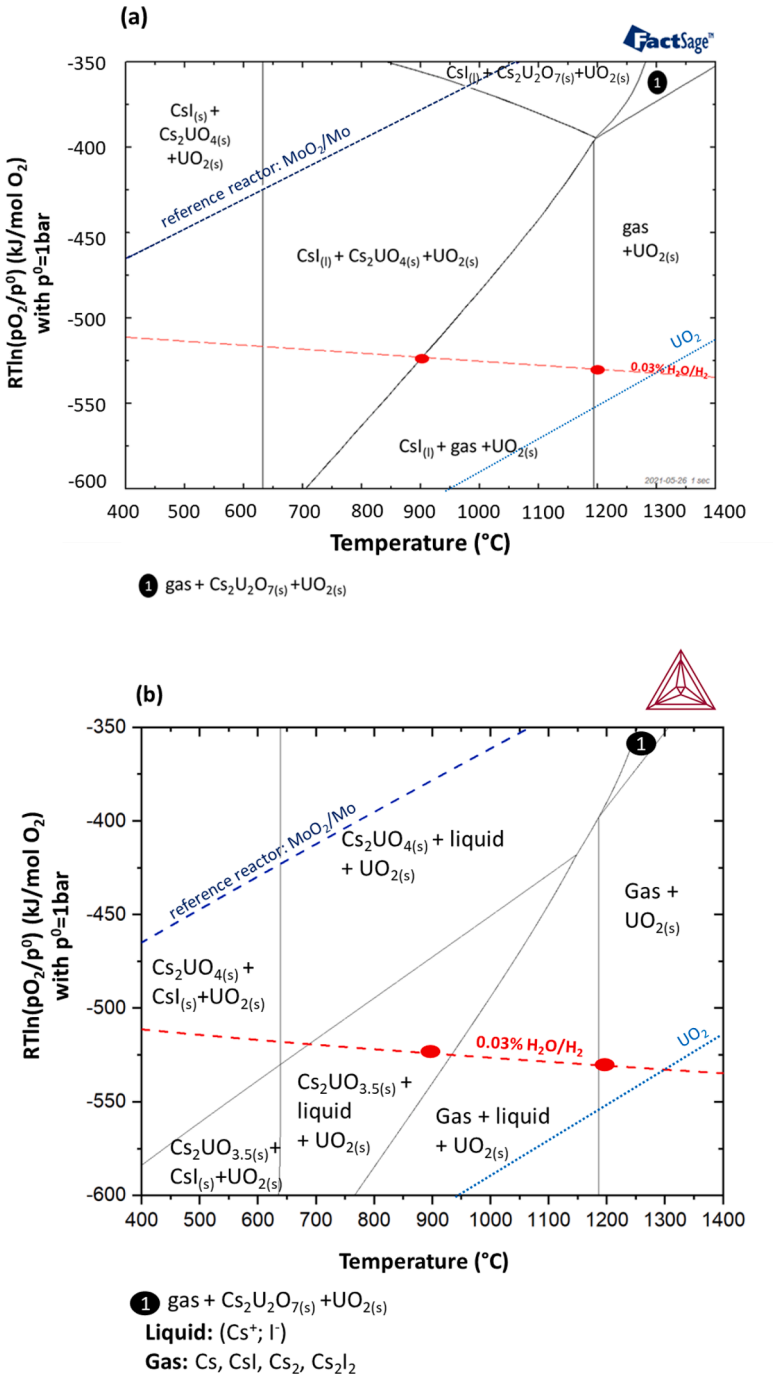

Fig. 2. Predominance diagrams of the system Cs-I-UO_2 for HC sample calculated by FactSage with the SGPS database (a) and Thermo-Calc with the TAF-ID database (b). The total pressure is 1 bar. The red dots represent the experimental conditions. The MoO_2/Mo and UO_2 equilibria lines are only indicated for positioning the evolution of the oxygen potential in the fuel under normal conditions.

0.4±0.2 nm) are present in the implanted part but also in the non-implanted part due to the FIB process. Their size and density are close to those of the defects produced by FIB (in a fresh sample). It is therefore not possible to discriminate between the FIB-induced vacancy type defects and those generated by the implantation process of I and Cs ions in this case. But, some published studies [29,30,24] show that nanoscale cavities or sub-nanoscale vacancy type objects can be evidenced after ion implantation (lamella prepared by other techniques or different FIB protocols). It is therefore likely that some sub-nanometric vacancy type objects such as those observed here were also induced by the I and Cs implantation but they may be not numerous enough compared to FIB induced defects to be clearly identified and discriminated from these latter.

Sample heat treated at 900°C.

After heat treatment at 900°C for 4 h (Fig. 5), substantially different defects have been observed and their distribution within the implanted layer is very inhomogeneous:

- precipitates: between 20 and 250 nm deep with a density of (4±1)·1021 m−3 and diameters between 5 and 15 nm (average diameter: 7 ±2 nm);
- bubbles/cavities:
  - nanometric (~ 1 nm diameter): near the surface (0 - 15 nm deep), probably due to a surface effect or to the migration of iodine and

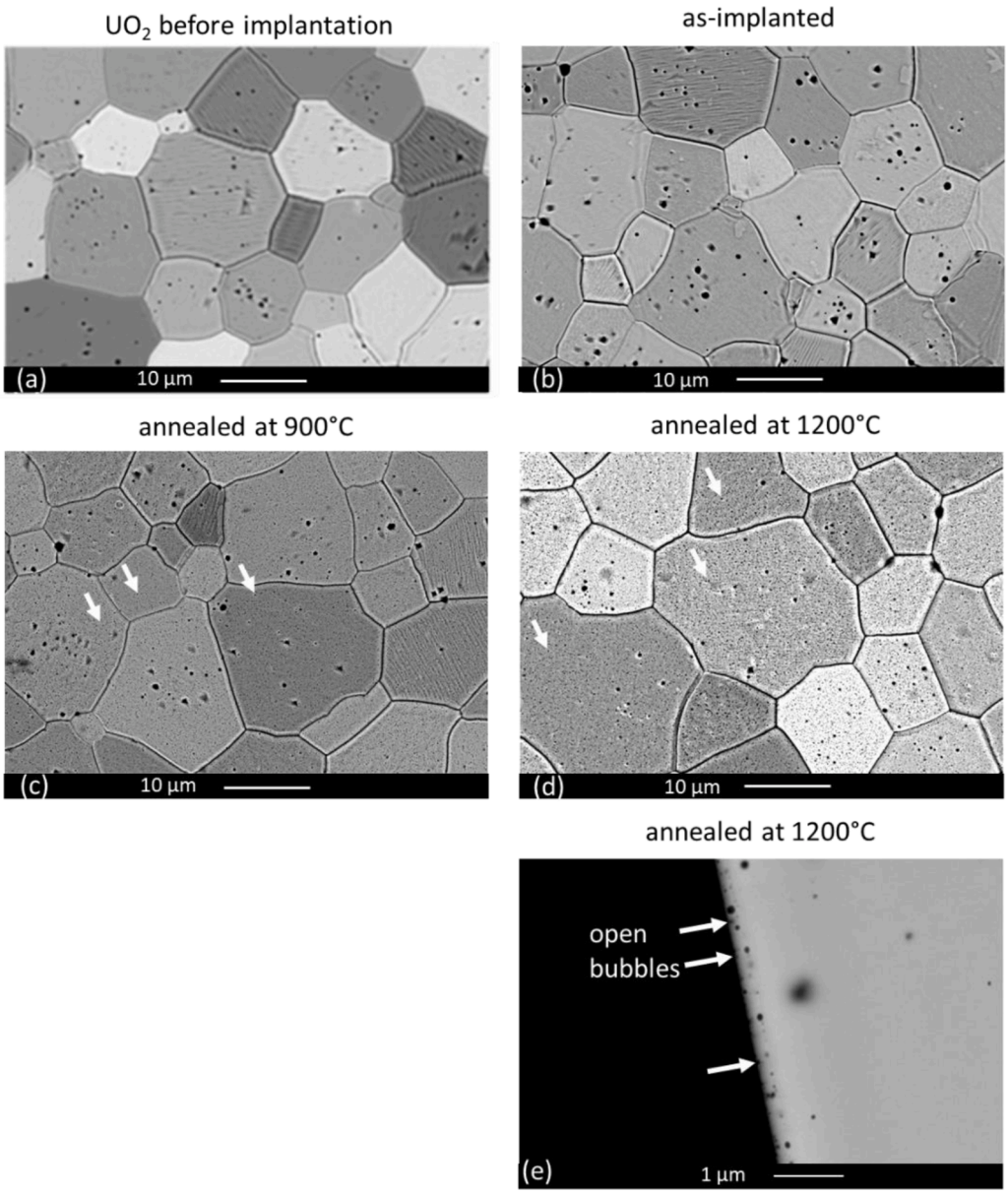

Fig. 3. SEM images of the HC sample: UO_2 before implantation (a), as-implanted (b), after annealing at 900°C (c) and after annealing at 1200°C (d). SEM image of the cross section of HC sample annealed at 1200°C (e). White arrows point on some open bubbles.

caesium towards the surface, and at the end of the implantation zone (350 - 400 nm deep) probably due to the annealing and/or clustering of a part of the implantation defects;

- clusters of nanometric bubbles (diameter < 2 nm) (blue rectangles): between 20 and 200 nm deep with an average density in the clusters of $(4\pm1)\cdot1024$ m−3 and an average diameter of 0.5 ± 0.3 nm;
- "large" bubbles: located between 5 and 200 nm below the surface with a density of $(5\pm1)\cdot1021$ m−3 and a diameter between 5 and 50 nm (average diameter: 12 ± 4 nm). Many bubbles exhibit a non-homogeneous contrast (different shades of grey). This contrast may be explained by the deposition of a condensed phase on the inner surface of these bubbles, or by the puncture of some bubbles during the preparation by FIB: indeed, the large bubbles seem partially punctured as if there were actually several bubbles stacked on top of each other (perpendicularly to the lamella surface) and only the one closest to the surface was punctured. Some of these bubbles are open at the implantation surface of the sample, thus confirming the SEM observations, whereas some others within the implanted layer are often anchored on dislocation lines;

- dislocations: between 50 and 300 nm depth, some dislocation lines can be observed, mostly anchoring bubbles, and between 250 and 400 nm a few large diameter ($\leq$ 10 nm) loops are also present. By comparing with the loops observed in the as-implanted sample, we can notice qualitatively that the loops seem to have grown and their density should have decreased. These dislocations correspond to implantation defects which remain after the heat treatment.

Sample heat treated at 1200°C.

After the heat treatment at 1200°C for 1 h (Fig. 6), we can observe the presence of:

- precipitates: between 250 and 350 nm deep, some precipitates are attached to dislocation lines (density: $(3\pm1)\cdot1021$ m−3; average diameter: 10 ± 3 nm);
- bubbles/cavities:

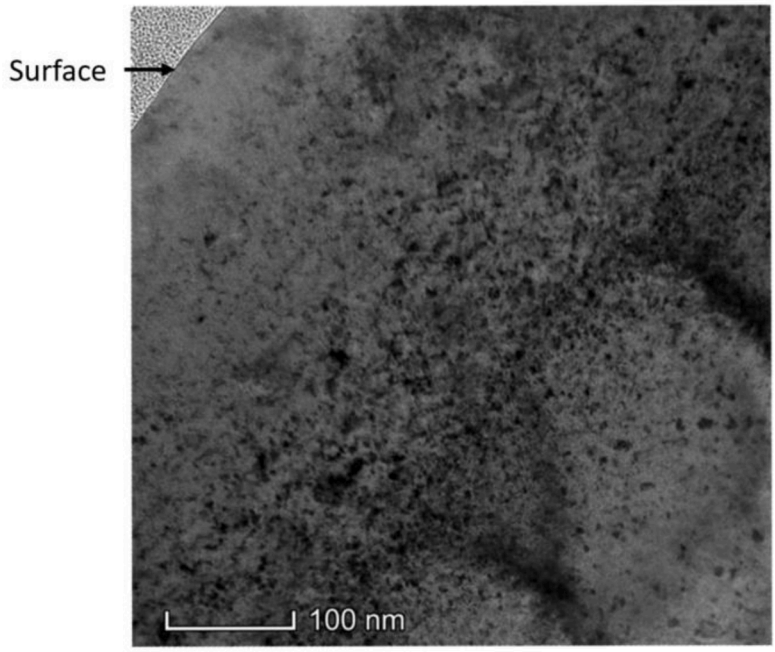

Fig. 4. Bright field TEM image of the HC sample after implantation ($\vec{g} = \langle 111 \rangle$).

- nanometric (~ 1 nm diameter): as for the other annealed sample, near the surface (0 - 15 nm deep) and at the end of the implantation zone (350 - 400 nm deep). An annealing and/or a clustering of implantation defects may have caused these nanometric bubbles/cavities;
- "large" bubbles: between 20 and 100 nm deep with an average density of (8±2)·1021 m−3 and diameters between 15 and 50 nm (average diameter: 24±6 nm). Some of these bubbles are open at the surface of the sample (confirming the SEM observations). Bubbles with a non-homogeneous contrast, similar to those present in the 900°C annealed sample, are also visible. A few bubbles and bubble stacks with diameters between 5 and 30 nm are observed between 200 and 350 nm depth, but anchored on dislocation lines;

- dislocations: some lines anchoring bubbles between 200 and 350 nm in depth. As for the 900°C annealed sample, these dislocations are the implantation defects residues after the heat treatment.

To summarize, our TEM study has evidenced important microstructure evolutions. Indeed, we observed:

- nanometric cavities/bubbles on the surface and at the end of the implanted zone (300 – 400 nm) for all the annealed samples. This type of objects are probably the results of annealing and/or clustering of implantation defects;
- partial annealing of dislocation-type defects (loop growth and interaction to form lines);
- an evolution of the size and distribution of the bubbles within the implanted zone : at 900°C cluster of nanometric bubbles are observed in addition to large bubbles, whereas at 1200°C only large bubbles remain. Moreover, after the heat treatment at 1200°C, the bubbles are located closer to the surface than those observed after the annealing at 900°C;
- the formation of precipitates, particularly during annealing at 900°C. Very few precipitates are visible after annealing at 1200°C.

3.3. Localization of implanted I and Cs in UO_2

Fig. 7 displays the evolution of I and Cs depth concentration profiles in UO_2 after implantation and after thermal treatments at 900°C and at 1200°C under controlled atmospheres, as deduced from SIMS analysis. It should be noticed that 5-7 profiles were acquired for each sample. Only the 2 profiles corresponding to the optimal conditions (described in §2.3.3.) are presented here. For each sample, all the profiles exhibited the same trends.

As-implanted profiles.

Firstly, depth profiles for as-implanted samples are consistent with SRIM calculations (Fig. 1) for the two elements with semi-Gaussian distributions. Nevertheless slight shifts of the concentration maxima towards shallower depths are observed (for I at 130 nm vs. 141 nm according to SRIM and, for Cs at 123 or 138 nm vs. 141 nm according to SRIM), as well as slightly lower concentrations at the maxima and also slight spreading of experimental profile with respect to SRIM calculations. These deviations can be explained by the dependence of the sputtering yield with the UO_2 crystal orientation: our UO_2 samples being polycrystalline, it results in a distribution of depths for a given abrasion time. The use of an eucentric rotating sample stage may help preventing this effect in future studies [31]. Moreover, it is to note that sample abrasion is slower using O_2^+ ions (to analyse Cs) than using Cs^+ (to analyse I), resulting in less reproducible measurements, and explaining the observed shift between the two Cs profiles.

Iodine depth profiles after thermal treatments.

The I profiles show a concentration maximum at 75 nm after 4h at 900°C and at 50 nm after 1h at 1200°C (Fig. 7 (a)). The profiles obtained after 4h at 900°C also exhibit a concentration plateau between 120 nm and 200 nm: iodine thus seems homogeneously distributed in this area. The profile 2 for the sample annealed at 1200°C also presents a small concentration plateau between 145 and 160 nm. Moreover, on the two profiles obtained on this sample, small fluctuations can be seen between 50 and 160 nm. These are probably due to an inhomogeneous sputtering of the grains, which is more visible in this sample whose iodine concentration is the lowest. Therefore, these results evidence a shift of the iodine concentration maximum with temperature, and more generally of the whole iodine profile, towards the surface with temperature and an absence of diffusion beyond the implanted zone.

Integrals of the I concentration profiles decrease significantly after the heat treatments. Calculations of release rates show a decrease of the iodine concentration of almost 35 % after 4h at 900°C and almost 74 % after 1h at 1200°C.

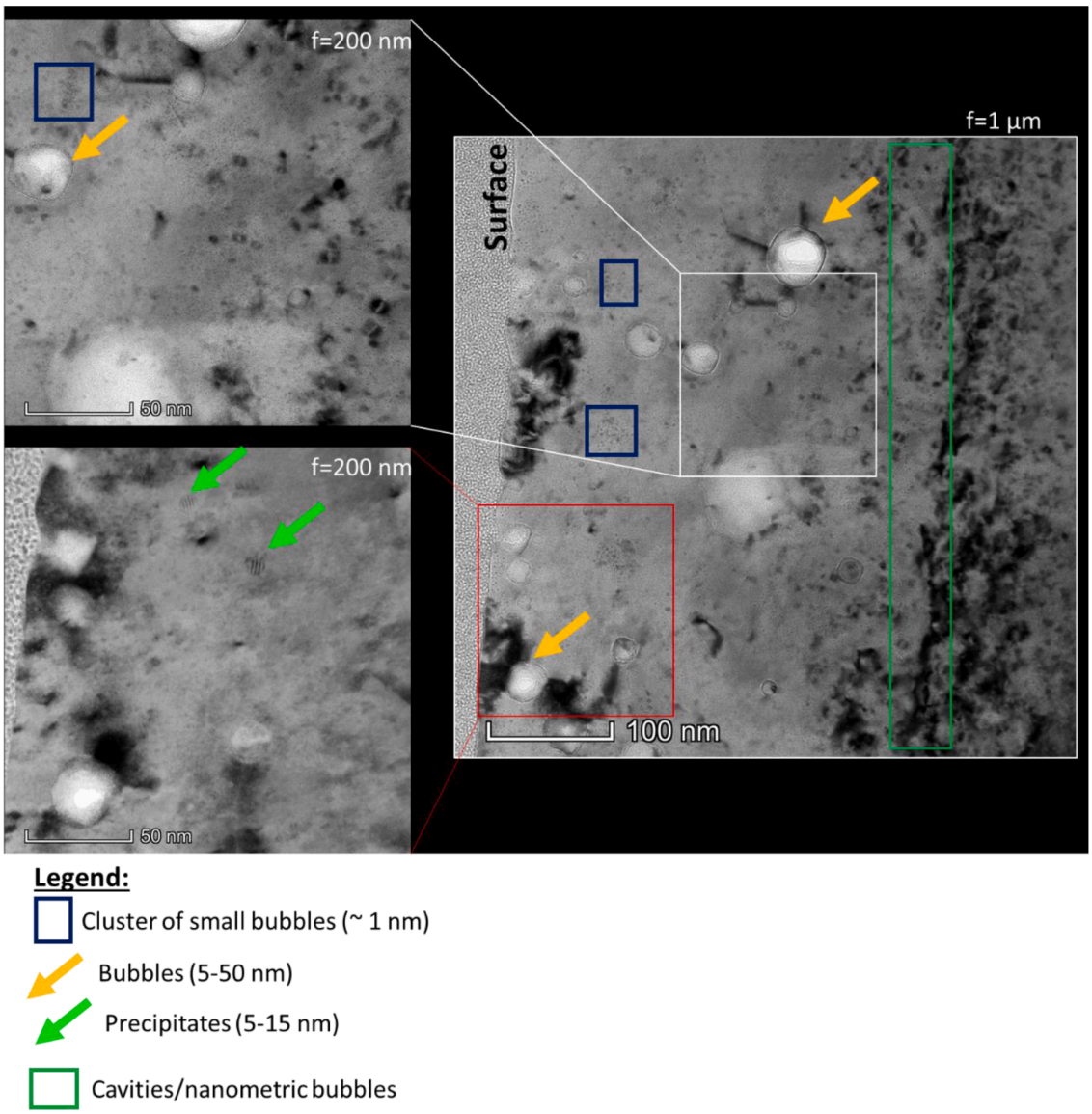

Fig. 5. Bright field TEM images in over-focused conditions of the HC sample after a heat treatment at 900°C during 4 h (f indicates focus).

Caesium depth profiles after thermal treatments.

The Cs profiles show a concentration maximum at around 75 nm after 4h at 900°C and at around 50 nm after 1h at 1200°C (Fig. 7 (b)). The profiles of the sample annealed at 1200°C exhibit a shoulder for profile 1 around 140 nm and a maximum of profile 2 around 180 nm. As for iodine, these results evidence a shift of the concentration maximum, and more generally of the whole caesium concentration profiles, towards the surface and an absence of diffusion beyond the implanted region. We can thus conclude that caesium migrates towards the surface under the effect of temperature.

The integrals of the Cs concentration profiles decreased significantly after the heat treatments. Calculations of the Cs release rates shows a decrease in total caesium concentration of nearly 50 % after 4h at 900°C and nearly 80 % after 1h at 1200°C.

Comparison of I and Cs concentration profiles.

The observations of I and Cs profiles after annealing show that the maximum concentrations of I and Cs are always located at the same depths for a given temperature. The I and Cs concentration profiles thus tend to overlap, which may traduce some interactions between the two elements.

Furthermore, no diffusion, neither of iodine nor of caesium, beyond the implanted region of the sample can be evidenced. It can be supposed that the irradiation-induced defects favour the diffusion of Cs and I in the implanted region UO_2, so that under the effect of temperature, caesium and iodine are able to migrate globally towards the surface.

It is interesting to note that, after 4h at 900°C, despite important release rates, the caesium concentration remains approximately twice as that of iodine, whereas after 1h at 1200°C, the iodine and caesium concentrations tend to almost equal values. This result is consistent with the possible formation of CsI at 1200°C. However, additional longer heat treatments would be necessary to consolidate this observation.

3.4. Speciation of Cs and I in UO_2

3.4.1. XANES results

XAS analysis was conducted on the HC and LC samples.

Iodine-L_3 edge.

Fig. 8 shows the I L_3 spectra of the as-implanted samples and a reference CsI spectrum. The spectrum of the as-implanted HC sample mainly exhibit a shoulder at 4567 eV and a bump at 4575 eV. The shoulder is less marked for the as-implanted LC sample and the bump is at 4579 eV for this sample. Reference spectra for an iodine atom inserted

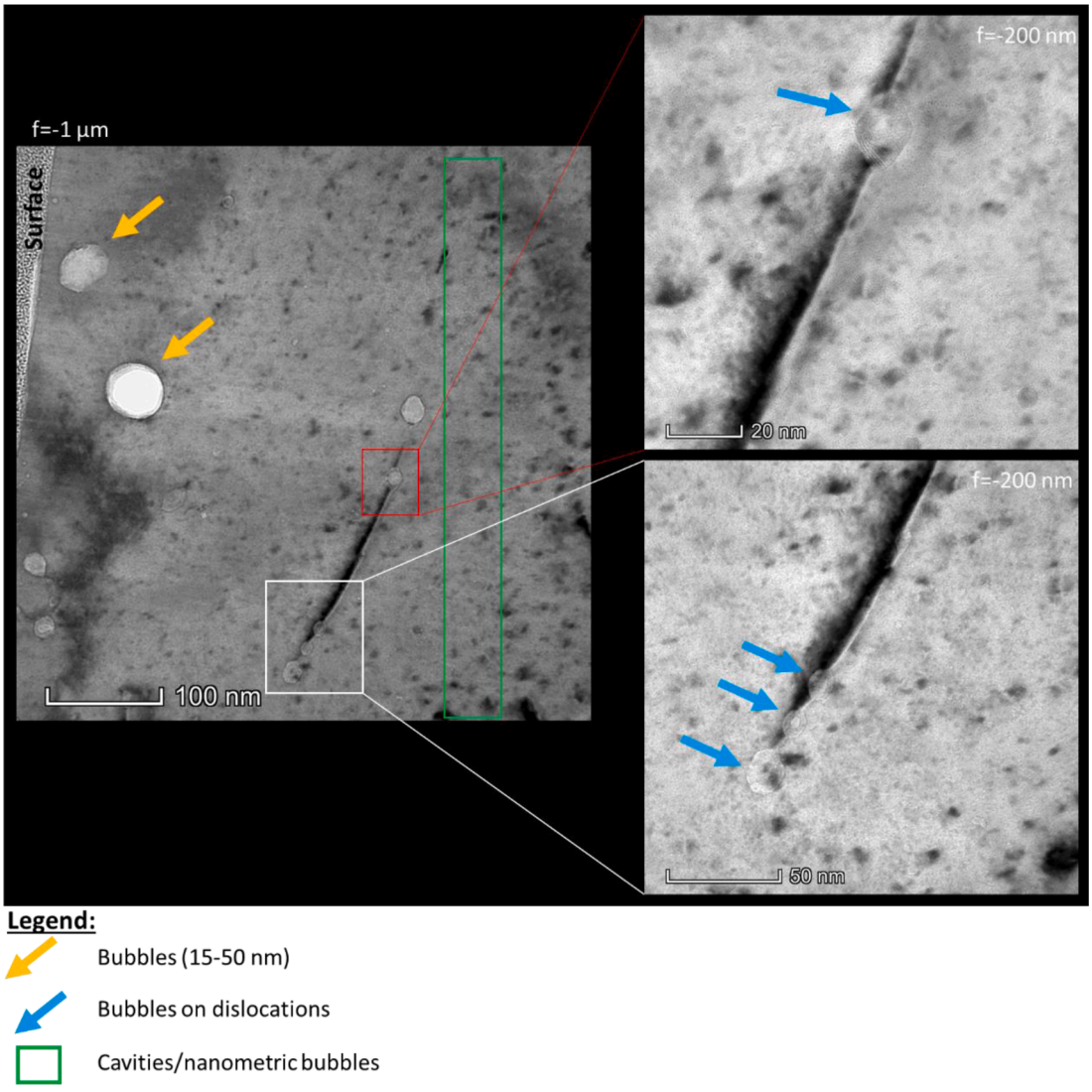

Fig. 6. Bright field TEM images of the HC sample after a thermal treatment at 1200°C during 1 h (f indicates focus).

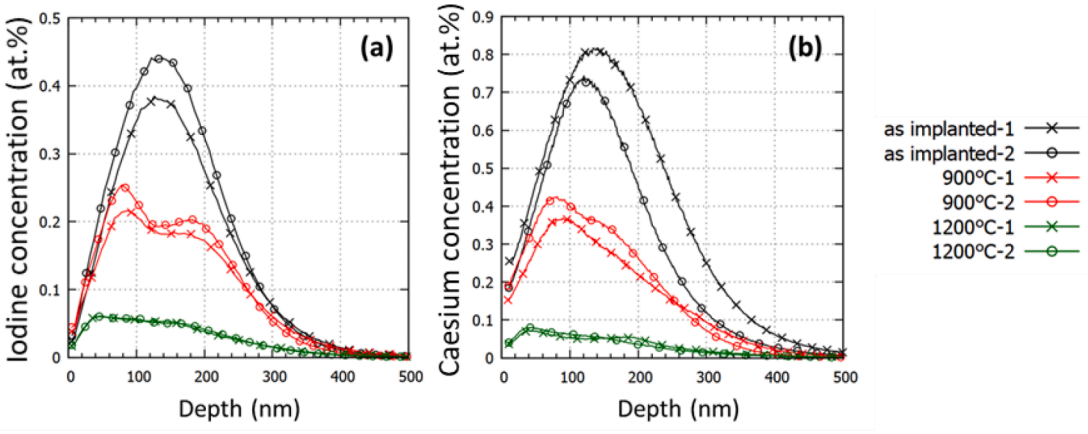

Fig. 7. Depth profiles obtained with SIMS on iodine (a) and on caesium (b) of IC samples as-implanted and annealed at 900°C during 4 h or at 1200°C during 1 h.

in various sites of the UO_2 fluorite structure (bound Schottky defects, U or O vacancies, interstitial) have been simulated with FDMNES code. Unfortunately, neither experimental nor simulated reference spectra could help yet successfully reproducing the as-implanted I L_3 spectrum: theoretical investigations are underway to explain its spectral features.

We observe significant differences between the spectra before and after thermal treatments, traducing an evolution of iodine speciation at high temperatures. The spectra for HC samples (Fig. 8(a)) after 4h at 900°C and 1h at 1200°C are almost identical and clearly show the iodine signature in the CsI compound, in good accordance with thermodynamic

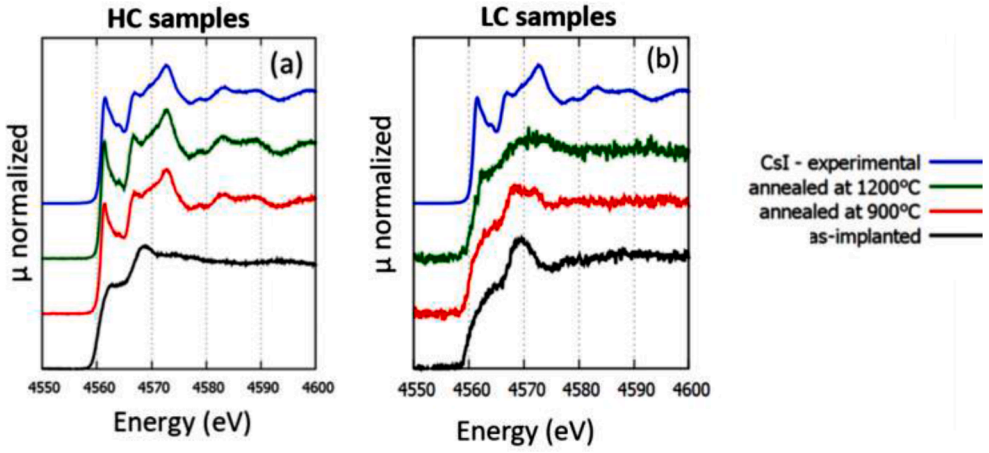

Fig. 8. I-L_3 edge XANES spectra of UO_2 implanted with Cs and I as-implanted and after 4h at 900°C or after 1h at 1200°C compared with reference spectrum of CsI: HC sample (a) and LC sample (b).

calculations. However, the pseudo-white line at 4562 eV is slightly more intense (and very slightly shifted, by about 1 eV, towards lower energies) in the co-implanted samples, probably reflecting the minor presence of iodine in another chemical form.

Fig. 8 (b) shows the spectra of the heat treated LC samples. Despite their more noisy character (due to the lower iodine concentration) we can note that they are different from the as-implanted spectrum, thus also confirming an evolution of speciation with temperature. However the spectra of the heat treated LC samples are quite different from those of the HC samples. We can observe a tendency to resemble that of CsI, in particular after 1h at 1200°C, with the appearance of an absorption peak at 4561 eV, the displacement of the maximum towards 4573 eV and the growth of a small bump around 4585 eV. The spectrum of the sample heat treated at 900°C has more similarities with the spectrum of the as-implanted sample (bumps at 4563 eV and 4595 eV). These results show that during the thermal treatment of the LC samples, part of the iodine reacted with Cs to form CsI while another part probably still remained in its as-implanted form. We can assume that a longer annealing time would allow the iodine to be fully converted into CsI.

Ceasium-L_3 edge.

Fig. 9 (a) shows the Cs L_3 spectra for the as-implanted samples and for CsI reference sample, as well as the simulated spectra of Cs_2UO_4 and metallic Cs. The spectrum of the as-implanted sample is mainly composed of one broad intense absorbance peak (so-called white line) at 5016 eV, and a small bump close to 5031 eV. The very similar spectral shapes of the LC and HC samples evidence the absence of significant Cs-Cs and Cs-I interactions during the implantation process. As for iodine L_3 edge, no matching reference spectrum could be found to help inferring the local environment of as-implanted Cs in UO_2, and theoretical investigations are also underway.

As for iodine, evolutions of the spectra are observed after thermal treatments. Similarities between the spectra of the samples heat treated at 900°C and at 1200°C can be seen: a white line at 5015 eV and bumps at 5020 eV and 5032 eV. Nevertheless, some differences are also noticeable: after 4h at 900°C, the white line at 5015 eV is less intense and the dip at 5018 eV is less marked if compared to the spectrum of the sample heat treated 1h at 1200°C. These differences evidence an evolution of Cs speciation at high temperature. The spectrum obtained with the sample heat treated at 1200°C overlaps almost perfectly with the reference spectrum of CsI: this unambiguously shows that most caesium forms CsI at 1200°C, in good accordance with thermodynamic calculations. For the sample heat treated at 900°C, the agreement is less perfect, but characteristic features (a white line at 5015eV, a bump at 5020 eV and a slight bump at 5033 eV) also clearly indicate the presence of CsI. The differences indicate the presence of at least another Cs-bearing phase. This observation is consistent with the SIMS results which still show twice as much caesium as iodine after 4h at 900°C, and is confirmed by thermodynamic calculations, which predict the formation of a caesium uranate (Cs_2UO_4 or $Cs_2UO_{3.5}$ depending on the database). Unfortunately, no experimental Cs L_3 XAS spectrum for such uranates is reported in literature. Thus, we have no way of verifying if our Cs_2UO_4 XANES simulation is correct. Moreover, no structural data to be used for XANES simulation can be found concerning $Cs_2UO_{3.5}$. The simulated spectrum of metallic Cs shows essentially a white line and no specific

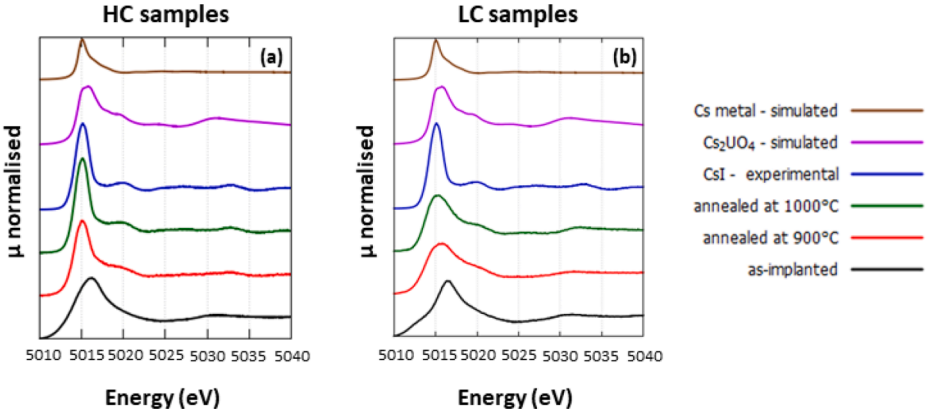

Fig. 9. Cs-L_3 edge XANES spectra of UO_2 implanted with Cs and I as-implanted and after 4h at 900°C or after 1h at 1200°C compared with reference spectrum of CsI and simulated XANES spectra of Cs_2UO_4 and of Cs metal: HC sample (a) and LC sample (b).

signature at higher energies so we cannot conclude on the presence of metallic Cs (corresponding to the condensed form at room temperature of gaseous Cs or Cs_2 whose formation at high temperature is predicted by the thermodynamic calculations). Finally, the Cs L_3 spectra do not show a lot of differences between the considered compounds (metallic Cs, CsI and Cs_2UO_4), so it is difficult to make reliable linear combinations from quite similar reference spectra.

Fig. 9 (b) shows the experimental spectra of the annealed LC samples compared with the experimental spectra of the as-implanted HC sample. In addition, the experimental CsI spectrum and the calculated spectra of Cs_2UO_4 and metallic Cs are shown. Firstly, we can notice that the spectra of the heat treated samples are also different from the spectrum obtained on the as-implanted sample, indicating again an evolution of Cs speciation during the thermal treatments. The spectra of the heat treated LC samples show some similarities with the spectrum of the HC sample annealed at 900°C, although broadened. These observations, coupled with those made at the I L_3 edge, confirm the majority presence of CsI in all the heat-treated samples. However, as in the HC samples, Cs is also present in at least one other chemical form, which may be the same as in the HC sample annealed at 900°C. Unfortunately, the present study does not allow us to conclude about their nature.

To conclude, XANES results unambiguously show the formation of CsI during the thermal treatments, which is the predominant phase after the heat treatment at 1200°C. The spectrum of the HC sample annealed at 900°C indicates that Cs should be present in at least another chemical form.

3.4.2. EDX results

The EDX analyses were carried out on lamellae of thermally treated HC samples using STEM mode. The elemental maps of these samples are presented in Figs. 10 and 11. Some of the U emission lines are missing in the Velox database but the missing lines are presented in [32]. These are very close to some I and Cs emission lines which makes it difficult to separate and unambiguously identify them. To overcome this lack and to determine qualitatively if I or Cs are present at a given location (precipitates or bubbles), we compared the EDX spectra obtained in the area of interest with a reference spectrum measured on the UO_2 matrix (Fig. 12 area 2). We considered the L_α (3.94 keV) emission line as the signature of the presence of iodine and $L_{\beta1}$ (4.62 keV) and $L_{\beta2}$ (4.93 keV) lines as signatures of caesium. The EDX spectra of the studied zones are presented in Fig. 12. Areas 1 and 3 for the sample heat-treated at 900°C and area 1 for the sample heat-treated at 1200°C correspond to bubbles. It was tricky to distinguish bubbles from precipitates in our samples with the HAADF detector. Thus, we identified the objects by means of conventional TEM.

After the heat treatments at 900°C and 1200°C, the TEM observations revealed bubbles and some precipitates. We can see in the EDX spectra of these objects the presence of a peak at 3.95 keV and of another one at 4.62 keV, corresponding to the L_α line of iodine and to the $L_{\beta1}$ of caesium. We can also observe the presence of a shoulder at 4.25 keV on the broad peak coming from the uranium M_3O_3, M_3O_5, M_3P_1 and M_1N_2 transitions, which also corresponds to the L_α line of caesium (Fig. 12). This observation evidences the co-localization of I and Cs within the bubbles, down to 300 nm depth for both heat treatments, and thus confirms the previous results. Noteworthy, we did not manage to detect I and Cs in the UO_2 matrix, confirming the very low solubility of these elements.

3.4.3. EELS results

The EELS analysis was performed using STEM mode on the two heat-treated HC samples. This mode has been chosen in order to have a probe size at least equivalent to the radius of the objects of interest. Only the spectra obtained on the sample heat treated at 1200°C are presented here (Fig. 13), those obtained on the sample heat-treated at 900°C being

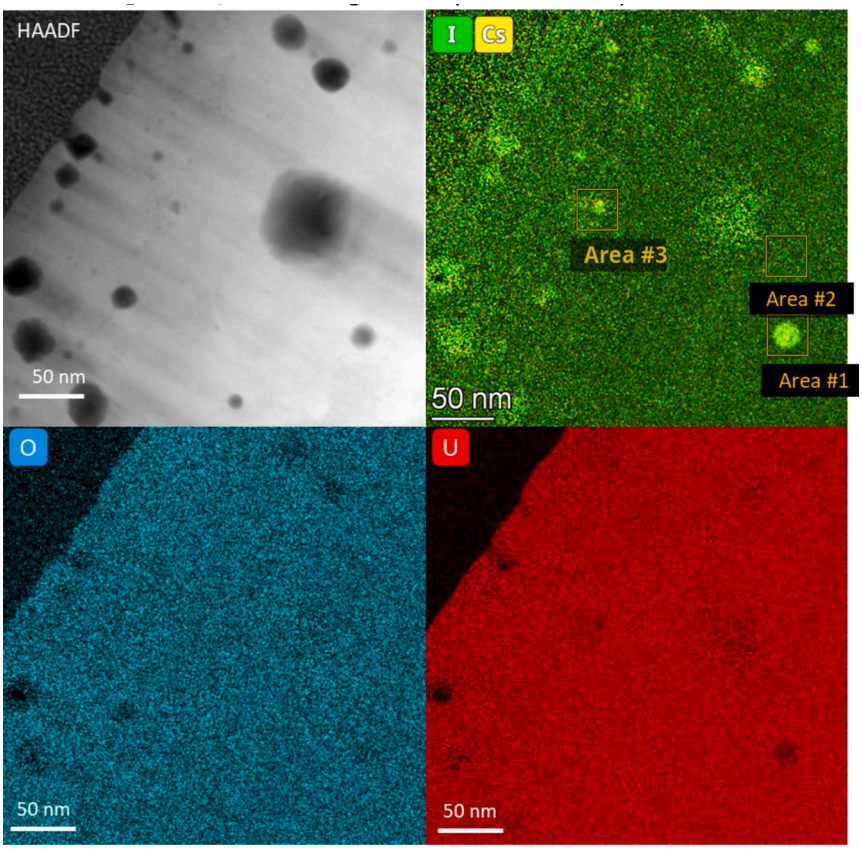

Fig. 10. HAADF picture and EDX map of I, Cs, O and U of the HC sample heat treated during 4 h at 900°C.

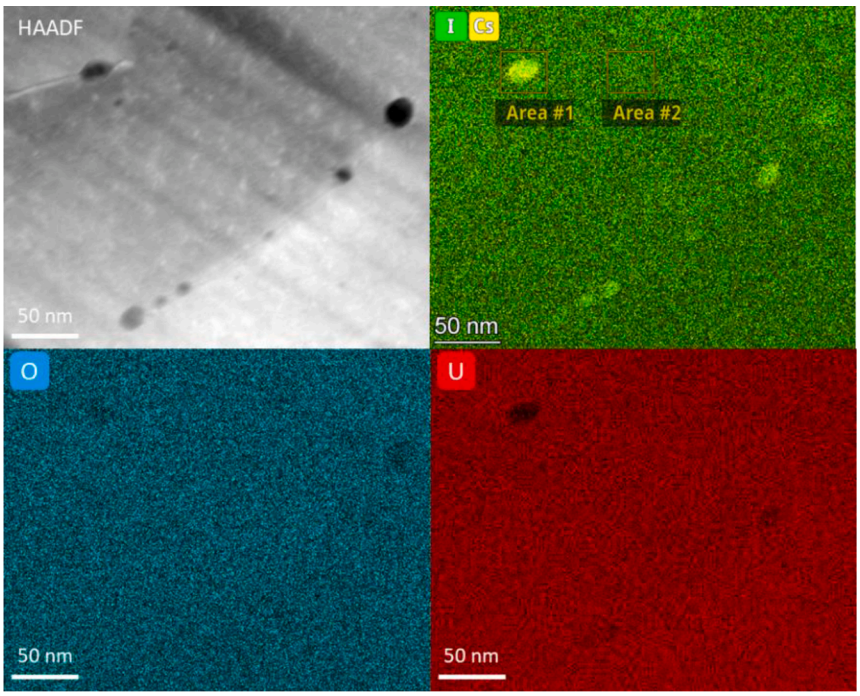

Fig. 11. HAADF picture and EDX map of I, Cs, O and U of the HC sample heat treated during 1 h at 1200°C.

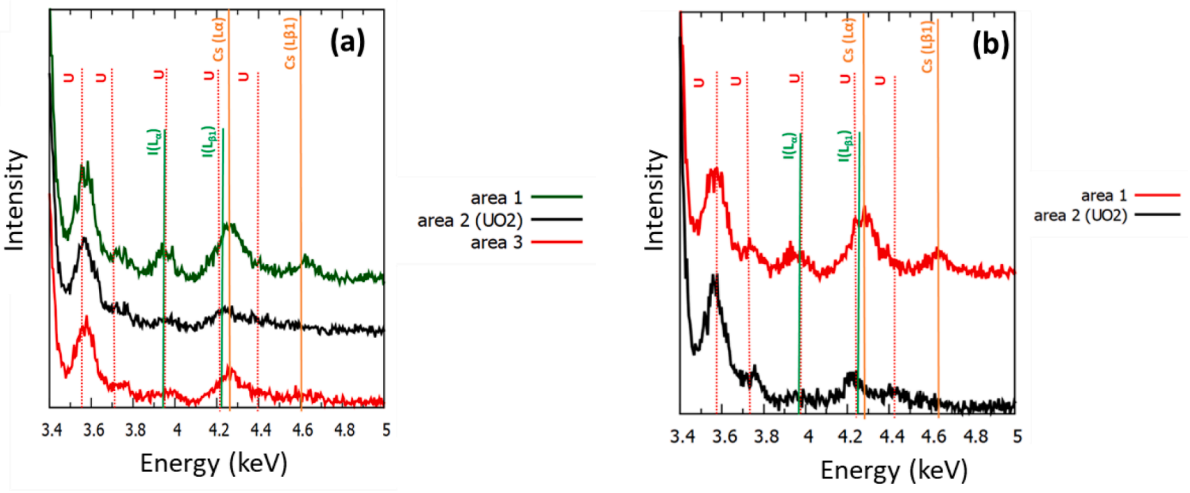

Fig. 12. EDX spectra obtained from the selected areas from Fig. 10 (a) and from Fig. 11 (b).

very similar. Due to the small difference in contrast between a bubble and a precipitate in the HAADF images, EELS spectra were first obtained on various objects, whose natures were identified afterwards in conventional TEM mode. As a result, we analysed four bubbles on each sample and the obtained spectra are all similar. The analyses of the precipitates were more complex: due to their small size (5-15 nm) and the probed size used, the contribution of the UO_2 matrix was larger than in the case of the bubbles for the obtained spectra. We could thus obtain no more pertinent information from this technique to determine the chemical nature(s) of these precipitates.

On Fig. 13, the spectrum (a) corresponds to the UO_2 matrix while the spectrum (b) corresponds to a bubble. We note the presence of the I and Cs edges, indicating their presence within the bubbles. In addition, the EELS spectrum obtained on the UO_2 matrix shows the absence of dissolved I and Cs or that the quantity is so small that we would be at the limit of detection. Hence these results confirm well the previous observations.

4. Discussion

TEM observations have indicated an important evolution of the microstructure with temperature as summarized in Fig. 14. We observed annealing of the implantation defects with increasing temperature. Indeed, initially only small dislocation loops were observed and after 1h at 1200°C, few dislocation lines are present and few larger loop remained, mostly anchored on bubbles and/or precipitates. In addition, large bubbles appear to grow during the heat treatments. Some of these bubbles have inhomogeneous contrasts with different shades of grey. These contrasts may suggest stacking of several bubbles (parallel to the observation direction) or a deposition of a condensed phase on the inner surface of the bubbles. Open bubbles at the sample surface are also visible, which are also observed by SEM. An evolution of the size of the

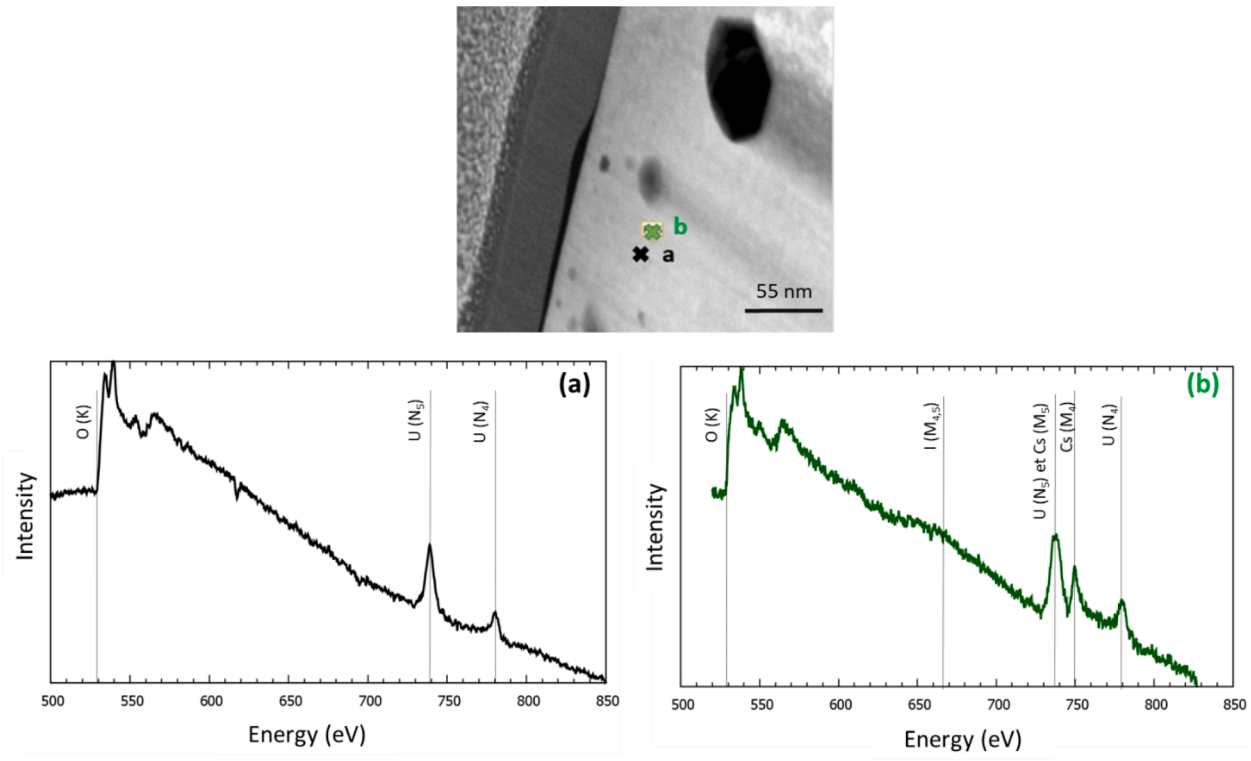

Fig. 13. HAADF image and EELS spectra from sample HC heat treated at 1200°C at different positions: (a) in the UO_2 matrix and (b) in a bubble containing Cs and I.

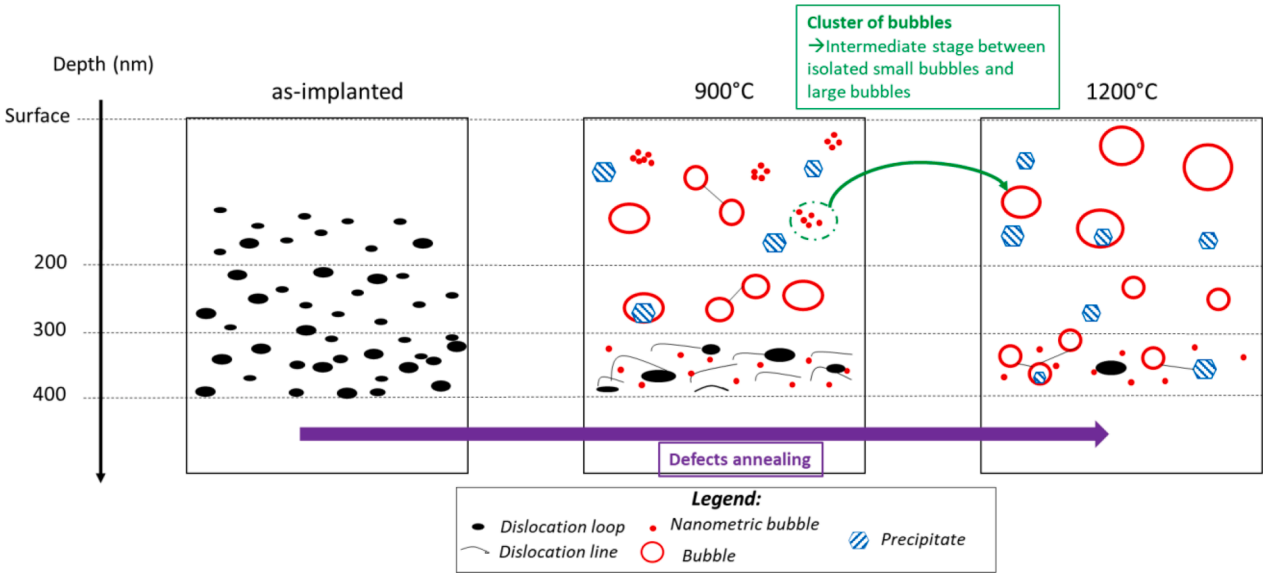

Fig. 14. Schematic illustration of the evolution of the microstructure of UO_2 lamellae implanted with Cs and I before and after annealing at 900°C and 1200°C.

bubbles with the annealing temperature is also deduced. Indeed, after annealing at 900°C, clusters of small (nanometric) bubbles are observed, whereas after annealing at 1200°C, larger bubbles (50-100 nm in diameter) are mainly seen. Therefore, these clusters of small bubbles seem to be the intermediate stage between isolated small bubbles and larger bubbles.

The SIMS results have shown changes in the concentration profiles with the heat treatment. We note that the concentration maxima of I and Cs migrate towards the surface and are always located at the same depths at a given temperature (Fig. 15). They did not diffuse beyond the implanted region, i.e. toward the bulk of the sample, due to the lack of solubility of these elements in the non-irradiated UO_2 matrix [33]. Furthermore, the I and Cs concentration profiles tend to overlap and equalize, in agreement with the formation of a compound of stoichiometry $(CsI)_x$.

The SIMS concentration profiles showed that some important gaseous releases occurred (nearly 50 % after 4h at 900°C and 90 % of implanted elements are lost after 1h at 1200°C) in agreement with the observations by SEM and TEM of open bubbles on the sample surface (Fig. 15). It should be noted that the release rate is higher for caesium than iodine. Additional thermal treatments would be required to determine the influence of the annealing time on the release rate, until

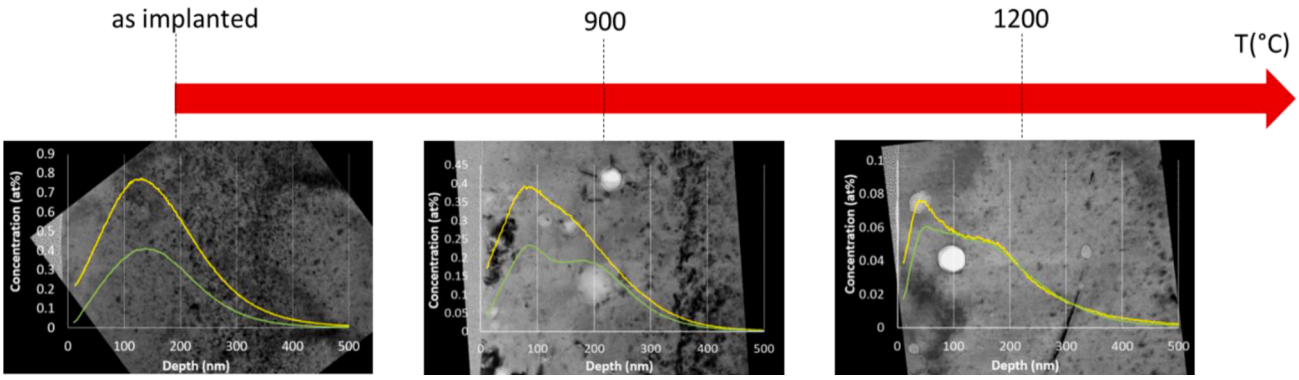

Fig. 15. Overlay of SIMS concentration profiles on TEM images for samples implanted with I and Cs, as-implanted at room temperature (left) and annealed at 900°C (middle) and 1200°C (right).

complete release is achieved (if possible).

The XANES analysis shows that iodine is mostly in the form of CsI. Furthermore, the EDX and EELS analyses confirm the presence of iodine and caesium in the bubbles. Such results clearly confirm the presence of CsI in the bubbles at 900°C. In addition, an *in situ* high temperature TEM and EELS analysis on the as-implanted sample revealed the presence of CsI in bubbles as early as 800°C [34]. Sekiguchi et al. also detected CsI (g) as early as 630°C in their tests to measure Cs and I partial pressures in fuels for molten salt reactors [35]. The occurrence of CsI in gas phase only at these temperatures is consistent with either a low total pressure in the bubbles (pressure local to a bubble) and/or a decrease of iodine content (loss during thermal treatment), which stabilizes gaseous form of CsI to the detriment of its condensed phase (cf. §. 3.1.).

XANES shows that, after thermal treatment, caesium is not only in the form of CsI but also in one or more other minor forms that we are still unable to identify, and whose proportion decreases with the temperature of the thermal treatment. The Cs profiles obtained by SIMS tend to overlap with those of iodine as the thermal treatment temperature increases. This confirms that, at equilibrium, part of Cs is fixed in the sample by I in the form of CsI. However, the question remains as to which other chemical forms Cs volatilizes. Observations tend to show that part of Cs released in the form of CsI, but the release rates of Cs are much higher than for I. As shown in Fig. 16, the condensed phases most likely to be formed in our experimental conditions (composition, pO_2 and temperature) are CsI(l) and Cs_2UO_4(s), in equilibrium with both CsI (g) and Cs(g) according to the following reactions: CsI(l) = CsI(g) and $Cs_2UO_4(s) = 2Cs(g) + UO_2 + O_2$. The equilibrium gas pressure of CsI(g) is a function of temperature only. That of Cs(g) depends on both temperature and O_2 partial pressure (cf. iso-pressure curves of Cs(g) in Fig. 16). According to thermodynamics, caesium is thus most likely to release as Cs_x(g), in addition to CsI(g), in our experimental conditions. Moreover, the amount of gaseous free caesium is predicted to decrease with temperature, which is consistent with the XANES observations.

In fact, the nature of the precipitates inside the samples may differ as a function of the cooling rate of the system until room temperature is reached and as said in § 2.1.3., the furnace used in this study did allow to have a precise control on the cooling. In that respect, two limiting cases are to be considered:

1 *The cooling was fast enough to prevent thermodynamic equilibrium of the sample:* the "high temperature" phases were therefore frozen by quenching and, then, precipitates of solid CsI and metallic Cs should be observable in the final samples. In this case, metallic Cs would result from the condensation of Cs(g) in the bubbles and Cs(s) would be expected to be systematically associated to gas bubbles after returning to room temperature;

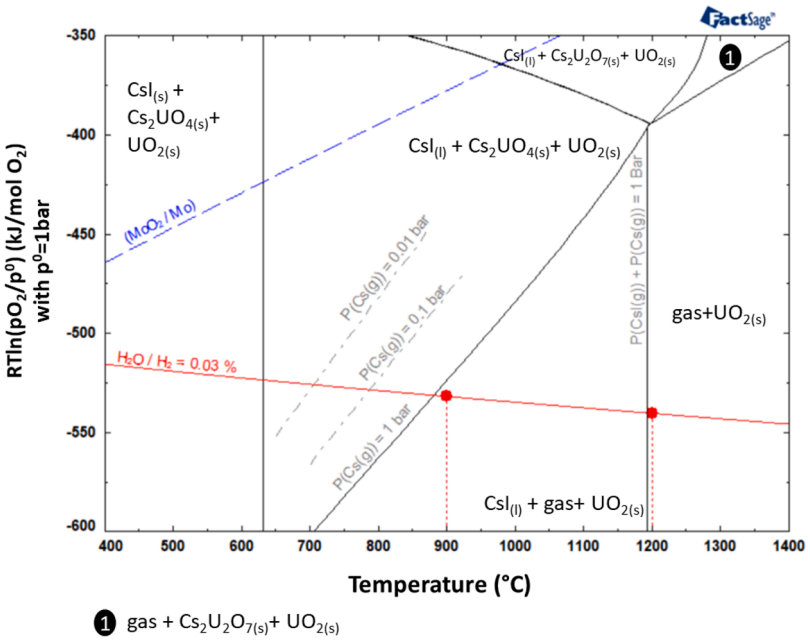

Fig. 16. Phase diagrams of the system Cs-I-UO_2 for HC sample calculated by FactSage with the review SGPS database.

2 *The cooling was slow enough for the sample to remain at the thermodynamic equilibrium*: then new phases may have formed at equilibrium at lower temperature. As a result, caesium uranate Cs_2UO_4 is likely to precipitate when temperature decreases together with solid CsI, according to thermodynamic predictions. In this case, caesium uranate would result from the direct interaction of Cs(g) with the UO_2 matrix and therefore precipitates should be found inside the sample matrix, close to bubbles, after returning to room temperature.

Our two samples annealed at 900°C and 1200°C both show precipitates dispersed in the UO_2 matrix with no apparent correlation with the gas bubbles. In addition, the XANES spectra both show some similarities with that of the simulated Cs_2UO_4 spectrum. These observations tend to be more consistent with the formation of a compound of caesium uranate type rather than metallic caesium. Further investigation are needed to fully confirm that assumption.

These results prove the great sensitivity of the studied systems to the heat treatment conditions, i.e. T and pO_2, which results in a more or less controlled evolution of the microstructures and speciation of the implanted elements during the tests. Special care must therefore be taken to ensure that:

- the thermodynamic equilibrium is effectively reached during annealing (longer annealing time);
- the evolution of the system during cooling is limited (very fast cooling rates or quenching).

5. Conclusion

This study focused on the interaction of I with Cs in UO_2. The coupling between an experimental approach and a modelling study allowed to highlight an evolution of the microstructure and speciation of caesium and iodine in UO_2 with thermal treatments (4 h at 900°C and 1 h at 1200°C with pO_2 set by 0.03% H_2O/H_2 equilibrium):

- microstructure: before heat treatment, the as- implanted sample had a high density of dislocation loops and sub-nanometric vacancy type objects. After heat treatment, these defects are still visible at lower densities. Moreover, we observed the formation of two types of bubbles: “large” bubbles (diameter between 5 and 100 nm) and clusters of small bubbles (diameter ~ 1nm). The cluster of small bubbles seems to be an intermediate stage between isolated small bubbles and “large” bubbles. Moreover, some open bubbles at the surface were visible, indicating gaseous releases during thermal treatments. Some small precipitates have been also observed (diameter between 5 and 15 nm);
- depth profiles: concentration peaks of Cs and I move together towards the surface with the temperature so there is co-localization of Cs and I. Furthermore, the concentration of the two elements decrease with the temperature of thermal treatment. This trend is more marked for Cs which indicated a higher release rate of this element;
- speciation: EDX and EELS results show the co-localization of Cs and I in bubbles and their absence in the matrix. XANES results show the formation of CsI and tend to indicate the possible formation of Cs2UOx (with x = 3.5 or 4).

The results confirmed the interaction of Cs and I at high temperature to form CsI mostly in the gas phase. The Cs in excess may be in the form of precipitates, probably Cs_2UO_4. However, according to calculations, Cs_2UO_4 should be stabilized only for the thermal treatment at 900°C. The formation of such a compound after a heat treatment at 1200°C would result from slow cooling rate allowing its stabilization at a lower temperature. Moreover, the concentration depth profiles showed a higher release rate in the case of Cs, which implies that an excess of Cs was released during thermal treatment, maybe partly in the form of Cs (g) or Cs_2(g).

CRediT authorship contribution statement

M. Rochedy: Investigation, Methodology, Writing – original draft. **V. Klosek:** Conceptualization, Investigation, Methodology, Writing – review & editing. **C. Riglet-Martial:** Conceptualization, Investigation, Methodology, Writing – review & editing. **C. Onofri-Marroncle:** Investigation, Methodology, Writing – review & editing. **D. Drouan:** Investigation. **D. Reyes:** Investigation, Methodology, Writing – review & editing. **P. Bienvenu:** Investigation, Methodology, Writing – review & editing. **I. Roure:** Investigation. **M. Cabié:** Investigation. **L. Amidani:** Investigation. **J. Léchelle:** Conceptualization, Investigation, Methodology, Writing – review & editing, Supervision. **M-A. Pinault-Thaury:** Supervision, Methodology.

Declaration of Competing Interest

The authors declare that they have no known competing financial interests or personal relationships that could have appeared to influence the work reported in this paper.

Data availability

Data will be made available on request.

Acknowledgements

The authors would like to thank EDF and FRAMATOME for their technical and financial support.

References

[1] M.H.A. Piro, D. Sunderland, S. Livingstone, J. Sercombe, W. Revie, A. Quastel, K. Terrani, C. Judge, A review of Pellet–Clad interaction behavior in zirconium alloy fuel cladding. Reference Module in Materials Science and Materials Engineering, Elsevier, 2017, https://doi.org/10.1016/B978-0-12-803581-8.09799-X.

[2] B. Baurens, Couplages thermochimie mécaniques dans le dioxyde d’uranium : application à l’ intéraction pastille-gaine, PhD Thesis, Université d’Aix-Marseille, 2014.

[3] L. Desgranges, C. Riglet-Martial, I. Aubrun, B. Pasquet, I. Roure, J. Lamontagne, T. Blay, Evidence of tellurium iodide compounds in a power-ramped irradiated UO_2 fuel rod, J. Nucl. Mater. 437 (2013) 409–414, https://doi.org/10.1016/j.jnucmat.2013.02.059.

[4] W.H. Hocking, R.A. Verrall, I.J. Muir, Migration behaviour of iodine in nuclear fuel, Nucl. Mater. 294 (2001) 45–52, https://doi.org/10.1016/S0022-3115(01)00447-0.

[5] C. Sabathier, L. Vincent, P. Garcia, F. Garrido, G. Carlot, L. Thome, P. Martin, C. Valot, *In situ* TEM study of temperature-induced fission product precipitation in UO2, Nucl. Instrum. Methods Phys. Res. B 266 (2008) 3027–3032, https://doi.org/10.1016/j.nimb.2008.03.158.

[6] L. Sarrasin, C. Gaillard, C. Panetier, Y. Pipon, N. Moncoffre, D. Mangin, R. Ducher, R. Dubourg, Effect of the oxygen potential on the Mo migration and speciation in UO2 and UO2+ x, Inorg. Chem. 58 (2019) 4761–4773, https://doi.org/10.1021/acs.inorgchem.8b03076.

[7] C. Panetier, L. Sarrasin, C. Gaillard, Y. Pipon, T. Wiss, A. Benedetti, AO. Dieste, D. Mangin, R. Dubourg, N. Moncoffre, Effect of molybdenum on the behaviour of caesium in uranium dioxide at high temperature, J. Nucl. Mater. 545 (2021), 152602, https://doi.org/10.1016/j.jnucmat.2020.152602.

[8] C. Panetier, Y. Pipon, C. Gaillard, N. Moncoffre, T. Wiss, D. Mangin, O. Dieste, B. Marchand, R. Dubourg, T. Epicier, L. Raimbault, Thermal behaviour of caesium implanted in UO2: a comparative study with the xenon behaviour, J. Nucl. Mater. 543 (2021), 152520, https://doi.org/10.1016/j.jnucmat.2020.152520.

[9] C. Panetier, Y. Pipon, C. Gaillard, D. Mangin, J. Amodeo, J. Morthomas, T. Wiss, A. Benedetti, R. Ducher, R. Dubourg, N. Moncoffre, Cs diffusion mechanisms in UO2 investigated by SIMS, TEM, and atomistic simulations, J. Chem. Phys. 156 (2022), 044705, https://doi.org/10.1063/5.0076358.

[10] D. Cubicciotti, S.M. Howard, R.L. Jones, The formation of iodine-induced stress corrosion cracks in zircaloys, J. Nucl. Mater. 78 (1978) 2–16, https://doi.org/10.13182/NT66-A27492.

[11] S.H. Shann, D.R. Olander, Stress corrosion cracking of zircaloy by cadmium, iodine, and metal iodides, J. Nucl. Mater. 113 (1983) 234–248, https://doi.org/10.1016/0022-3115(83)90148-4.

[12] B. Cox, Pellet-clad interaction (PCI) failures of zirconium alloy fuel cladding-a review, J. Nucl. Mater. 172 (1990) 249–292, https://doi.org/10.1016/0022-3115(90)90282-R.
[13] J.C. Wood, Factors affecting stress corrosion cracking of zircaloy in iodine vapour, J. Nucl. Mater. 45 (1972) 105–122, https://doi.org/10.1016/0022-3115(72)90178-X.
[14] B. Cox, R. Haddad, Methyl iodide as a promoter of the SCC of zirconium alloys in iodine vapour, J. Nucl. Mater. 137 (1986) 115–123, https://doi.org/10.1016/0022-3115(86)90040-1.
[15] P. Hofmann, J. Spino, Chemical interactions between simulated fission products and zircaloy-4 at elevated temperatures, including influence on ductility and time-to-failure, J. Nucl. Mater. 102 (1981) 117–134, https://doi.org/10.1016/0022-3115(81)90552-3.
[16] R. Kohli, Chemical Thermodynamics of Complex Systems: Fission Product Behavior in LWR Fuel Elements, Lawrence Berkeley National Laboratory, 1981.
[17] Ziegler, J.F., Biersack, J.P., Littmark, U. The stopping and range of ions in solids, in: D.A. Bromley (Ed.), Treatise on Heavy-Ion Science, Springer, Boston, MA, 1985, doi:10.1007/978-1-4615-8103-1_3.
[18] J. Soullard, High-voltage electron-microscope observations of UO2, J. Nucl. Mater. 135 (1985) 190–196, https://doi.org/10.1016/0022-3115(85)90077-7.
[19] C. Guéneau, N. Dupin, L. Kjellqvist, E. Geiger, M. Kurata, S. Gossé, E. Corcoran, A. Quaini, R. Hania, A.L. Smith, M.H.A. Piro, T. Besmann, P.E.A. Turchi, J. C. Dumas, M.J. Welland, T. Ogata, B.O. Lee, J.R. Kennedy, C. Adkins, M. Bankhead, D. Costa, TAF-ID: an international thermodynamic database for nuclear fuels applications, Calphad 72 (2021) 102212, https://doi.org/10.1016/j.calphad.2020.102212.
[20] CW. Bale, E. Bélisle, P. Chartrand, S.A. Decterov, G. Eriksson, A.E. Gheribi, K. Hack, I.-H. Jung, Y.-B. Kang, J. Melançon, A.D. Pelton, S. Petersen, C. Robelin, J. Sangster, P. Spencer, M-A.Van Ende, Reprint of: FactSage thermochemical software and databases 2010–2016, Calphad 55 (2016) 1–19, https://doi.org/10.1016/j.calphad.2016.07.004.
[21] D.B. Williams, C.B. Carter, Transmission Electron Microscopy, Springer, 1996.
[22] B. Yao, D.J. Edwards, R.J. Kurtz, G.R. Odette, T. Yamamoto, Multislice simulation of transmission electron microscopy imaging of helium bubbles in Fe, J. Electron Microsc. (Tokyo) 61 (2012) 393–400, https://doi.org/10.1093/jmicro/dfs065.
[23] A. Michel, Etude de la précipitation de l'hélium dans les combustibles nucléaires UO2 et (U, Pu)O2 en condition de stockage, Thèse, PhD Thesis, Université Aix-Marseille (2019).
[24] C. Onofri, C. Sabathier, G. Carlot, D. Drouan, C. Bachelet, C. Baumier, M. Gérardin, M. Bricout, Changes in voids induced by ion irradiations in UO2: *in situ* TEM studies, Nucl. Instrum. Methods Phys. Res. B 463 (2020) 76–85, https://doi.org/10.1016/j.nimb.2019.11.031.
[25] R.G. Wilson, Secondary ion mass spectrometry sensitivity factors versus ionization potential and electron affinity for many elements in HgCdTe and CdTe using oxygen and cesium ion beams, J. Appl. Phys. 63 (1988), 51215125, https://doi.org/10.1063/1.340413.
[26] A.B. Van Egmond, Investigations on cesium uranates—V: the crystal structures of Cs_2UO_4, $Cs_4U_5O_{17}$, $Cs_2U_7O_{22}$ and $Cs_2U_{15}O_{46}$, J. Inorg. Nucl. Chem. 38 (1976), https://doi.org/10.1016/0022-1902(76)80653-7.
[27] Y. Joly, X-ray absorption near edge structure calculations beyond the muffin-tin approximation, Phys. Rev. B 63 (2001) 125120–125129, https://doi.org/10.1103/PhysRevB.63.125120.
[28] B. Ravel, M.A. Newville, ATHENA, ARTEMIS, HEPHAESTUS: data analysis for X-ray absorption spectroscopy using IFEFFI, J. Synchrotron Radiat. 12 (4) (2005) 537–541, https://doi.org/10.1107/S0909049505012719.
[29] L.F. He, B. Valderrama, A.R. Hassan, J. Yu, M. Gupta, J. Pakarinen, H. B. Henderson, J. Gan, M.A. Kirk, A.T. Nelson, M.V. Manuel, A. El-Azab, T.R. Allen, Bubble formation and Kr distribution in Kr-irradiated UO_2, J. Nucl. Mater. 456 (2015) 125–132, https://doi.org/10.1016/j.jnucmat.2014.09.026.
[30] L.F. He, X.M. Bai, J. Pakarinen, B.J. Jaques, J. Gan, A.T. Nelson, A. El-Azab, T. R. Allen, Bubble evolution in Kr-irradiated UO_2 during annealing, J. Nucl. Mater. 496 (2017) 242–250, https://doi.org/10.1016/j.jnucmat.2017.09.036.
[31] P.M.L. Hedberg, P. Peres, F. Fernandes, N. Albert, C. Vincent, Latest improvements in isotopic uranium particle analysis by large geometry–secondary ion mass spectrometry for nuclear safeguards purposes, J. Vac. Sci. Technol. B 36 (2018) (2018) 03F108, https://doi.org/10.1116/1.5017027.
[32] J. Dellith, A. Scheffel, R. Terborg, M. Wendt, Reinvestigation of the M emission spectrum of uranium-92, Microsc. Microanal. 17 (2011) 296–301, https://doi.org/10.1017/S1431927611000067.
[33] H. Kleykamp, The solubility of selected fission products in UO_2 and (U, Pu)O_2, J. Nucl. Mater. 206 (1993) 82–86, https://doi.org/10.1016/0022-3115(93)90236-R.
[34] M. Rochedy, Caractérisation expérimentale des produits de fission corrosifs dans UO2: étude du système (I-Cs-Te)-UO2, Thèse Université Paris-Saclay (2022).
[35] Y. Sekiguchi, K. Uozumi, T. Koyama, T. Terai, Fundamental study on the vaporization of cesium and iodine dissolved in LiF-NaF-KF molten salt, J. Nucl. Mater. 522 (2019) 136–143, https://doi.org/10.1016/j.jnucmat.2019.05.014.